Geophysical Research Letters

RESEARCH LETTER
10.1029/2018GL081592

Sensitivity Kernels of *PP* Precursor Traveltimes and Their Limitations for Imaging Topography of Discontinuities

Maria Koroni[1], **Hanneke Paulssen**[2], **and Jeannot Trampert**[2]

[1]Department of Earth Sciences, ETH Zürich, Zürich, Switzerland, [2]Department of Earth Sciences, Universiteit Utrecht, Utrecht, The Netherlands

Key Points:
- We present a sensitivity analysis of *PP* precursor traveltimes to clarify the reasons of their reported poor detectability
- The Fréchet derivatives show that the sensitivity to topography is weak, but high to the compressional and shear wave structure
- The usability of *PP* precursor traveltimes for imaging discontinuity topography is limited, given their weak sensitivity to boundary changes

Supporting Information:
- Text S1
- Text S2
- Text S3

Correspondence to:
M. Koroni,
maria.koroni@erdw.ethz.ch

Citation:
Koroni, M., Paulssen, H., & Trampert, J. (2019). Sensitivity kernels of PP precursor traveltimes and their limitations for imaging topography of discontinuities. *Geophysical Research Letters*, *46*. https://doi.org/10.1029/2018GL081592

Received 7 DEC 2018
Accepted 12 DEC 2018
Accepted article online 27 DEC 2018

Abstract We analyze the sensitivity of *PP* precursor traveltimes that are often used to infer lateral variation in the depths of the 410- and 660-km discontinuities in the mantle. Previous results were inconclusive due to complex wave phenomena, such as multiple energy conversions and focusing/defocusing, that hamper their interpretation. Using spectral-element synthetics and Fréchet derivatives calculated with adjoint methods, we compute sensitivity kernels for volumetric and boundary parameters in a 1-D model for representative epicentral distances of past studies, and a dominant period of 11–25 s. Our results indicate that the boundary sensitivity of *PP* precursors is low and that these phases are not coherently seen in exact synthetics. Our most important finding is the strong sensitivity to both shear and compressional wave speeds, indicating that wave interference and wave conversions are dominant. The *PP* precursor traveltimes appear more sensitive to structural parameters, that is, compressional and shear wave speed, than to the boundaries; therefore, they are unlikely sources for valuable insight into discontinuity topography.

Plain Language Summary Seismologists frequently use traveltimes of seismic waves to understand how the Earth's internal structure changes at various depths. This study presents pictorial examples of how traveltimes of seismic waves sense the depth variations inside the Earth. We focus on waves that reflect from specific depths, and they are often used to explain topography along interfaces at 410- and 660-km depths. Along these depths, the ambient mantle conditions change significantly, indicating areas of major changes in material distribution, which enable vigorous movements within the Earth and cause geological phenomena observed at the surface. We aim at explaining why resulting models using these traveltimes are not in agreement. To achieve that, we use exact methods that give an accurate picture of the sensitivity of the traveltimes under investigation. Our contribution is important because we visualize many effects relating to how the waves travel, convert, and interact with each other. These effects, if not taken into account in an exact manner, could lead to inaccurate mapping of topography. Our explanations can help seismologists understand the reasons of disagreement between models produced using these traveltime data. We conclude that further interpretations relating to temperature and compositional variations should be considered with great care.

1. The *PP* Precursors

PP precursors have thoroughly been investigated in the past due to their interaction with upper-mantle structure and their potential importance for imaging mantle discontinuity structure (e.g., Bolt, 1970; King et al., 1975; Ward, 1978). Studies have aimed at determining the sharpness, velocity, and density variations of the discontinuities found at approximately 410- and 660-km depth that define the mantle transition zone (e.g., Chambers et al., 2005a, 2005b; Deuss, 2009; Deuss et al., 2006; Flanagan & Shearer, 1999; Lessing et al., 2014; Neele & de Regt, 1999; Neele & Snieder, 1992; Schmerr & Thomas, 2011; Wajeman, 1988). Observations of long period *PP* precursors (15–75 s) were used to infer the topography of discontinuities globally (e.g., Flanagan & Shearer, 1999), while shorter-period data have been employed in more regional studies (Thomas & Billen, 2009). Knowledge of the topographic structure of the discontinuities at 410- and 660-km depth is important, because it can put strong constraints on the variations of temperature and composition as well as on the nature of the phase transitions of the mantle minerals present at those depths (e.g., Bina & Helffrich, 1992; Helffrich, 1999; Helffrich & Bina, 1994; Jeanloz & Thompson, 1983).

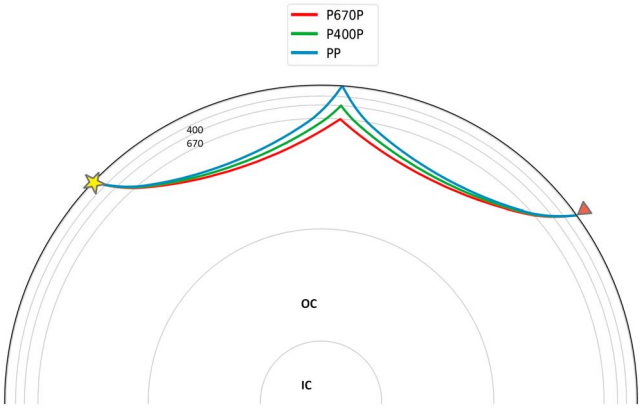

Figure 1. The theoretical raypaths of the *PP* phase and its precursors. OC denotes outer core, and IC inner core. Here the epicentral distance between source (yellow star) and receiver (red triangle) is equal to 110° . The precursors follow similar paths to the main phase and bounce off the underside of the mantle transition zone discontinuities.

The precursors to the *PP* phase are low amplitude signals arriving a few minutes before the *PP* phase. Similarly to the *SS* precursors, the *PP* precursors are interpreted as underside reflections off the bottomside of the 410 and 660 discontinuities. The similarity of their ray paths with the main *PP* phase allowed researchers to assume, within a ray theoretical framework, that their traveltimes are mainly sensitive to the structure beneath the surface reflection bounce point (Figure 1). The precursors may thus provide information about the structure and topography of the discontinuities, which can then be used for imaging. However, the small slowness difference between *PP* and its precursors observed in array studies led to speculations that the precursors could also be asymmetric reflections of the *PP* phase or appear due to scattering from heterogeneities in the upper mantle and crust (e.g., King et al., 1975; Wright, 1972; Wright & Muirhead, 1969). Nevertheless, the *PP* precursors have mainly been interpreted as the result of underside reflections off the global discontinuities at 410- and 660-km depth.

Within a linearized ray theoretical framework, depth estimation of the discontinuity at the bounce point can be made by measuring differential traveltimes, that is, t_{PP}–t_{PdP}, d being the depth of the discontinuity. Conventional methods rely on corrections of these traveltimes for the structural effects and draw inferences by interpreting the residual time anomaly as a result of depth variation of the discontinuity.

Despite in theory being an important type of data, ray theoretical traveltime studies of *PP* precursors obtained rather diverging results. This holds true both for global and regional studies of discontinuities (e.g., Lessing et al., 2015). The main difficulty is their poor detectability in real data. To enhance the visibility of these phases, researchers necessarily relied on stacking techniques by summing waveforms aligned to the *PP* phase (e.g., Deuss, 2009; Flanagan & Shearer, 1998, 1999; Rost & Thomas, 2002; Thomas & Billen, 2009), and several models have been derived using them (Chambers et al., 2005b; Deuss et al., 2006; Shearer & Flanagan, 1999). Despite stacking methods, the *P660P* precursor phase has not consistently been observed, if at all (e.g., Deuss, 2009; Lessing et al., 2014).

Several reasons for the poor detectability of *PP* precursor phases have been proposed: Estabrook and Kind (1996) suggested that the compressional wave velocity contrast is much lower at the 660 discontinuity than predicted by many global seismological models. Another explanation is that lateral mineralogical variations along the 660 could lead to some variability of the traveltimes resulting in inefficient stacking of waveforms (e.g., Deuss, 2009; Lessing et al., 2015). The topographic variations along the discontinuities themselves distort the waveforms of precursors, which results in a similar inefficient stacking. Finally, the long wavelength topography, which can vary by some tens of kilometers in amplitude, can cause defocusing of the precursor phases, affecting their amplitude significantly. A comprehensive study of the effects of topographic structure on *PP* precursor waves can be found in Neele and Snieder (1992, 1997). Previous analyses of the *P* wave coda have suggested that the energy conversion from *S* to *P* and vice versa can affect the waveform between the *P* and *PP* phases (Ward, 1978). Additional contributions to the coda of the *P* wave may also stem from asymmetric reflections at the mantle discontinuities as proposed by Wright (1972) and Schimmel (1997).

The use of geometrical optics in the interpretation of traveltimes of underside reflections neglects the shape of their associated Fresnel zone (e.g., Chaljub & Tarantola, 1997; Neele et al., 1997). The Fresnel zone of underside reflections, such as the *PP* and *SS* precursors, is a wide and extended area that spans thousands of kilometers and has a characteristic *X* shape. Therefore, it is expected that structures off the theoretical ray path may significantly contribute to the traveltimes of underside reflections. However, this is not properly accounted for when using ray theory. Thus, any traveltime interpretation based on geometrical optics may suffer from biases due to contributions from various wavelength structures. In addition, as shown in Koroni and Trampert (2016) for the *SS* precursors, the simple traveltime corrections are not sufficient to account for the effect of strong wave interference or reliably infer topographic variations assuming linearity of the traveltime data (Koroni et al., 2017).

The key questions we ask in this study are as follows: How sensitive are the *PP* precursors traveltimes to the boundaries at 410- and 660-km depth, and what is their sensitivity to compressional as well as shear velocity structure? For this sensitivity analysis we calculated Fréchet derivatives using adjoint methods (Talagrand & Courtier, 1987; Tarantola, 1984; Tromp et al., 2005). This approach allows us to visualize the exact sensitivity of *PP* traveltime precursors and investigate their suitability for interpretation in terms of discontinuity topography.

2. Experimental Setup and Methods

We performed the sensitivity analysis for stations located at an epicentral distance range between 90° and 150° from the earthquake source. We focus here on the distance of 110° . This epicentral distance is commonly included in studies involving *PP* precursors, since it limits interference from other phases, such as the *PKP* and multiples within the transition zone (Deuss, 2009; Neele & Snieder, 1992; Shearer & Flanagan, 1999). The sensitivity kernels for other characteristic distances are presented in the supporting information.

The synthetic data are calculated using an earthquake occurring at 20-km depth, with a source time function of zero duration. The moment tensor chosen here corresponds to a pure strike-slip mechanism, and the moment magnitude is 7.9. The vertical components used in this study have been filtered between the frequency band of 4 and 45.4 mHz. The above settings and processing lead to seismograms with a dominant period of about 25 s. The selection of these parameters is based on criteria favored by previous studies using precursor data. The selection of a delta source time function results in sensitivity kernels that are unfiltered, meaning that they may appear oscillatory, especially around the locations of source and receiver, due to the high spatial frequency content. We also computed sensitivity kernels for a longer duration of the source time function, which leads to a longer dominant period (close to 50 s), and the results remain similar. This is also true for seismograms with higher dominant frequencies. Examples are provided in the supporting information accompanying this article.

The simulations are performed with the spectral-element code SPECEM3D_GLOBE (Komatitsch, 2003; Komatitsch & Tromp, 2002a, 2002b), which allows for the calculation of exact, noise-free seismograms. The Earth parameters for ellipticity, self-gravitation, rotation, attenuation, and oceanic load are switched off to reduce the complexity of the synthetic waveforms. The Fréchet derivatives for traveltimes of *PP* precursors are computed using the adjoint method (Talagrand & Courtier, 1987), which has been formulated for seismological problems mainly by Tarantola (1984, 1987, 1988) and Tromp et al. (2005). The derivatives correspond to the banana-doughnut kernels (e.g., Dahlen et al., 2000; Marquering et al., 1998, 1999), which take into account the finite frequency nature of the signals. We use the 1-D model PREM (Dziewoński & Anderson, 1981) both for generating the synthetic data and as a background model for the adjoint simulations. Therefore, we hereafter refer to the discontinuities with their fixed depth in PREM, namely, 400 and 670 km. In the supporting information, we present kernels in different background models, which show overall the same patterns.

The cross-correlation traveltime anomaly within a given time window is sensitive to the boundary perturbation and volumetric parameters as shown in the following generic expression:

$$\delta T_s = \int_V (K_\alpha \, \delta \ln \alpha + K_\beta \, \delta \ln \beta) \, d^3x + \int_\Sigma K_r \, \delta \ln r \, d^2x. \tag{1}$$

In the expressions above, $\delta \ln \alpha$ and $\delta \ln \beta$ denote relative perturbations of the compressional and shear wave speeds, respectively. The relative perturbation of the radius of the discontinuity depth is given by $\delta \ln r$. The

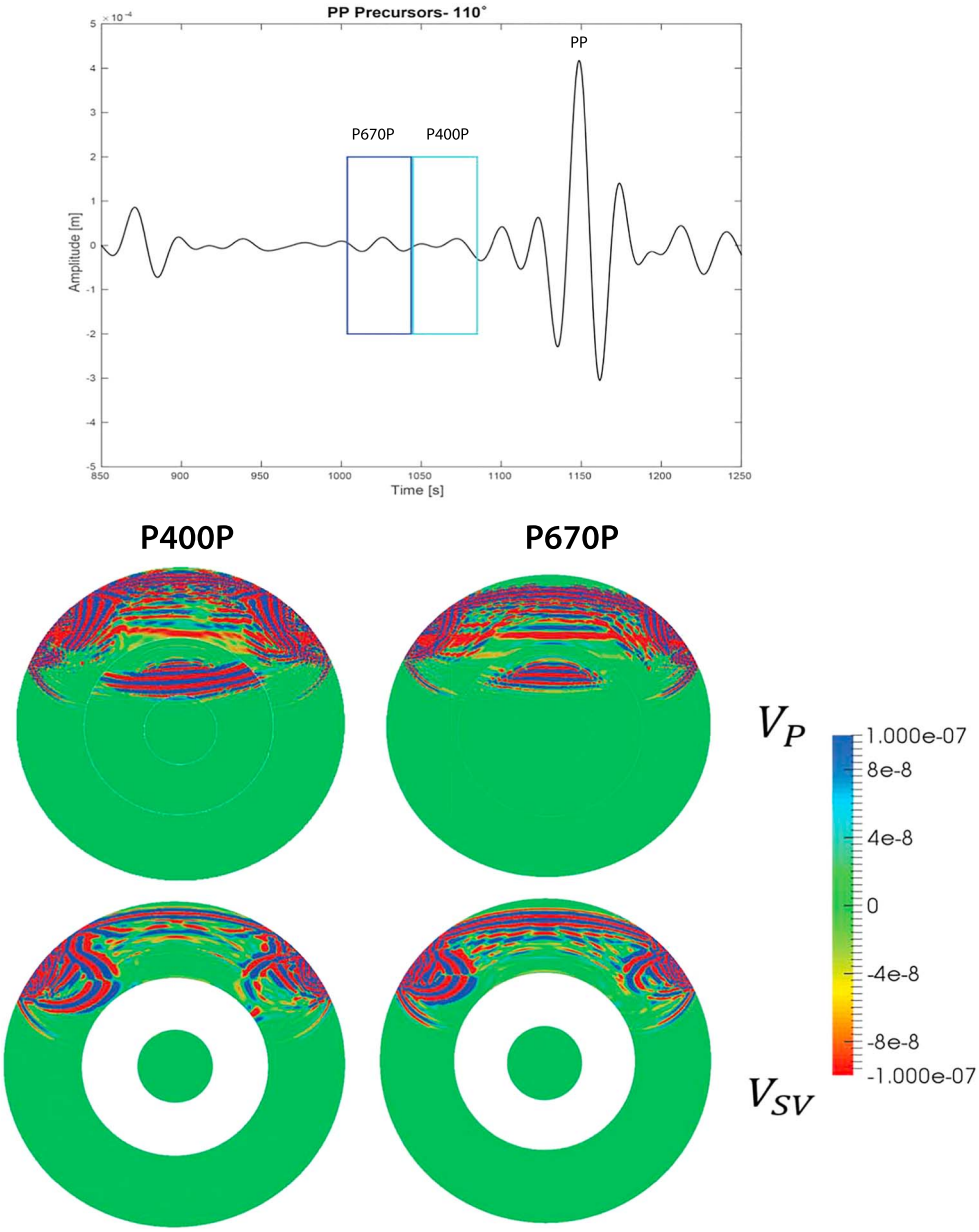

Figure 2. Top panel: synthetic, noise-free vertical component PREM seismogram at an epicentral distance of 110° showing the time windows used for calculating the kernels. Middle panel: volumetric sensitivity to compressional wave speed (V_P) for the *P400P* and *P670P* precursors. The regions separated by the thin white circles correspond to mantle, outer, and inner core. Bottom panel: volumetric sensitivity to shear wave speed (V_{SV}). The two regions shown are the mantle and inner core, separated by the zero-sensitivity outer core (white). Notice the overall sensitivity of the traveltimes due to many interfering waves. The units of the volumetric kernels are (s/km^3).

traveltime anomaly, denoted by δT_s, is thus due to a relative perturbation of the compressional and/or shear wave speed integrated over the volume V and/or a relative perturbation of the radius of the discontinuity integrated over the the surface Σ and is observed at the specific station s. The volumetric and boundary kernels have units of (s/km^3) and (s/km^2), respectively, and are presented in the following section.

3. Fréchet Sensitivity Kernels of *PP* Precursor Traveltimes

Figure 2 shows a vertical component seismogram for PREM with the selected time windows of the precursors for a station at an epicentral distance equal to 110° (top panel). The volumetric sensitivity kernels

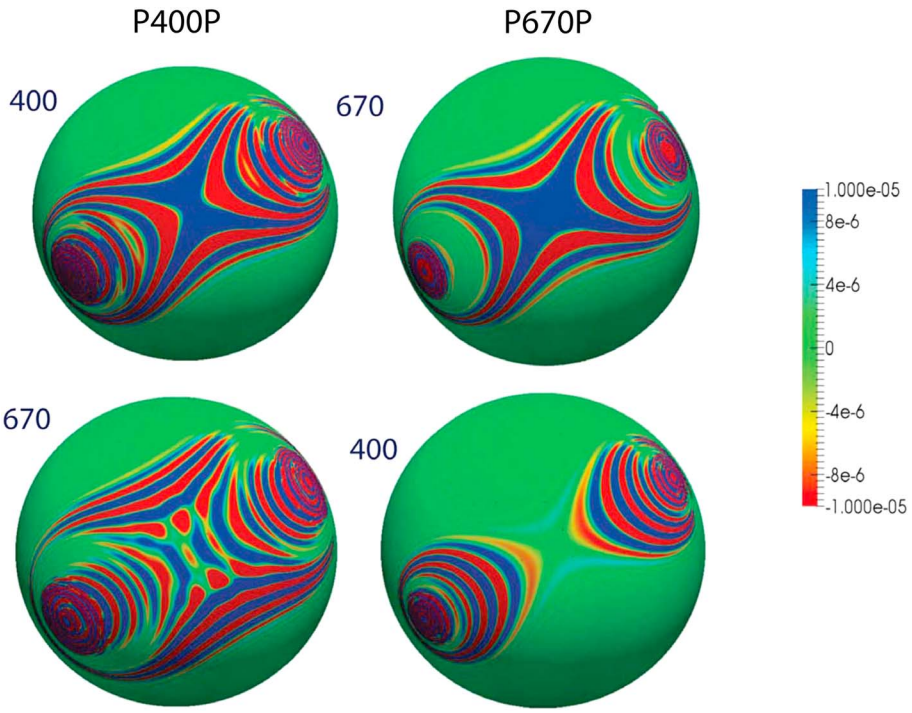

Figure 3. Top panel: boundary sensitivity of the *P400P* and *P670P* precursors to the 400 km (left) and 670 km (right) discontinuities. Bottom panel: the cross-sensitivity of the *P400P* and *P670P* to the 670- and 400-km boundaries, respectively. The units of the boundary kernels are (s/km^2).

for the *PP* precursor traveltimes are calculated with respect to compressional and shear wave speeds (middle and bottom panels). The volumetric V_P kernels show a strong interference from many waves. There is an influence from P_{diff}, and there is a strong presence of core phases. We also recognize symmetrical topside reflection legs of possible reverberations between the 400 and 670 discontinuities. The sensitivity of the precursors is very complicated with no distinct sensitivity to underside reflection paths as suggested from raypaths on Figure 1.

The bottom panels of the figure show that the precursor traveltimes exhibit an equally strong sensitivity to the shear wave speed V_{SV}, something that to our knowledge has not been particularly stressed in previous studies using *PP* precursors. This demonstrates that conversions between *P* and *S* wave energy are considerable and significantly affect the traveltimes of *PP* precursors. In the supporting information we show that *P* and *S* wave speed anomalies contribute about equally to the traveltime anomaly. This observation is consistent for both the *P400P* and *P670P* phases at this distance. More examples for other characteristic distances are provided in the supporting information, showing similar features. Notice also the relatively low sensitivity near the ray theoretical bounce point location.

In the supporting information, we also provide sensitivity kernels with respect to density. They show sensitivity mostly to mantle interfaces. These kernels will trade off with wave speed kernels but are potentially useful in the context of full waveform inversion.

The boundary sensitivity of the traveltimes of the *P400P* and *P670P* precursors is shown in Figure 3. The top panel of the figure shows that the *PP* precursors exhibit the characteristic *X*-shaped sensitivity, which covers a large area. It is notable that the amplitude of this sensitivity is very low compared to that for *SS* precursors (Koroni et al., 2017, and Figure 4). The bottom panel of Figure 3 shows the cross-sensitivity (i.e., *P400P* to the 670 discontinuity and *P670P* to the 400 discontinuity) with amplitudes that are comparable to those at the top panel. Such cross-sensitivity was also found for the *SS* precursors (Koroni et al., 2017). In the supporting information we show that at the midpoint location, where the maximum sensitivity is expected from ray theory, almost zero sensitivity is observed for certain epicentral distances.

Based on these observations, our results suggest that the sensitivity of the *PP* precursor traveltimes is complicated and dominated by sensitivity to both compressional and shear wave speeds, an observation that has

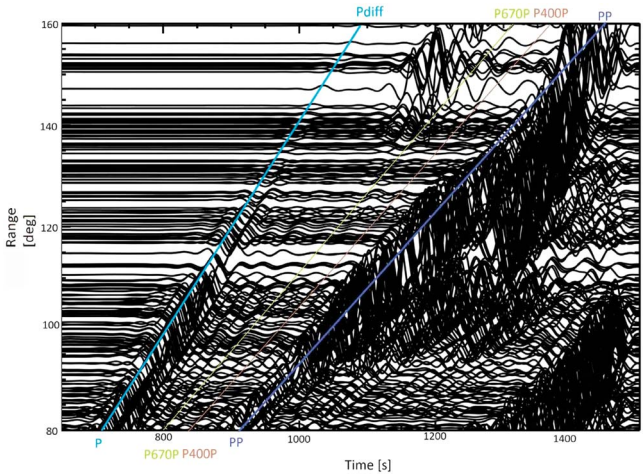

Figure 4. Top: vertical component seismogram with the time windows of *PP* the precursors. Below the corresponding 400 (left-hand side) and 670 boundary kernels are shown. Bottom: transverse component seismogram for the same station with the time windows of the *SS* precursors and the corresponding boundary kernels. The kernels are plotted with the same scaling to illustrate the difference in sensitivity amplitude. The kernel units are s/km^2.

important implications for corrections of traveltime data for structural effects. There is a prominent interference of topside reflections from the mantle discontinuities and of core phases in these volumetric kernels, which masks the signal related to the underside reflections, assumed to be dominant in all interpretation. We also calculated kernels for a longer source time function, which modifies the frequency content of the waveforms and prefilters the sensitivity kernels, as well as for higher frequencies. We find that the main observations are unchanged with changing the frequency content of the waveforms (see the supporting information). Regarding the boundary sensitivity of *PP* precursor traveltimes, we demonstrated that their sensitivity is considerably weaker than for *SS* precursors.

4. Discussion

The results presented in the previous section explain the difficulties related to observing and interpreting *PP* precursors. In the synthetic, noise-free waveforms used here, there are no clearly distinguishable peaks in the windows around the ray theoretical travel times of the *P400P* and *P670P* precursors. This is a consistent observation across a large distance range as can be seen in the record section plotted in Figure 5 and on a slant stack shown in the supporting material. Given that the precursor signal is not consistently observed, inferences on topographic structure or other parameters such as impedance and velocity jumps based on traveltimes of *PP* precursors should be carefully assessed and considered.

Difficulties in observing clear peaks are likely due to wave interference and conversions between *P* and *S* waves that arrive between the *P* and *PP* phases. More specifically, the *Ps400Pp*, *Pp670p*, and *Pp400p* phases may interfere with *P670P* (Husebye & Madariaga, 1970; Schimmel, 1997; Ward, 1978), or the near source upper-mantle phases *s400P*, *s670P*, *s400pP*, and *s670pP* reported by Ward (1978) could be major contributors, thus obscuring the *P400P* and *P670P* phases that already have weak amplitudes.

Usually, the waveforms are stacked in order to eliminate the bulk of wave interference and to enhance weak amplitudes. We created slant stacks to investigate whether there is coherent energy corresponding to the underside reflections. Using exact synthetics in PREM, we find that the precursors do not stack to significant amplitude, as shown in the contour plot in the supporting information. Therefore, stacking does not necessarily improve the usability of *PP* precursors in discontinuity studies.

It has to be mentioned that more powerful array methods (Rost & Thomas, 2002, 2009; Rost & Weber, 2002) can help dealing with wave interference as interfering phases may be identified and isolated from the *PP* precursors. Stacking techniques, such as velocity spectral analysis (Davies et al., 1971) or frequency-wavenumber methods (Schneider et al., 2018) employed in array studies, are capable of detecting signals that correspond to the *PP* precursors by significantly reducing interference of other phases. Although

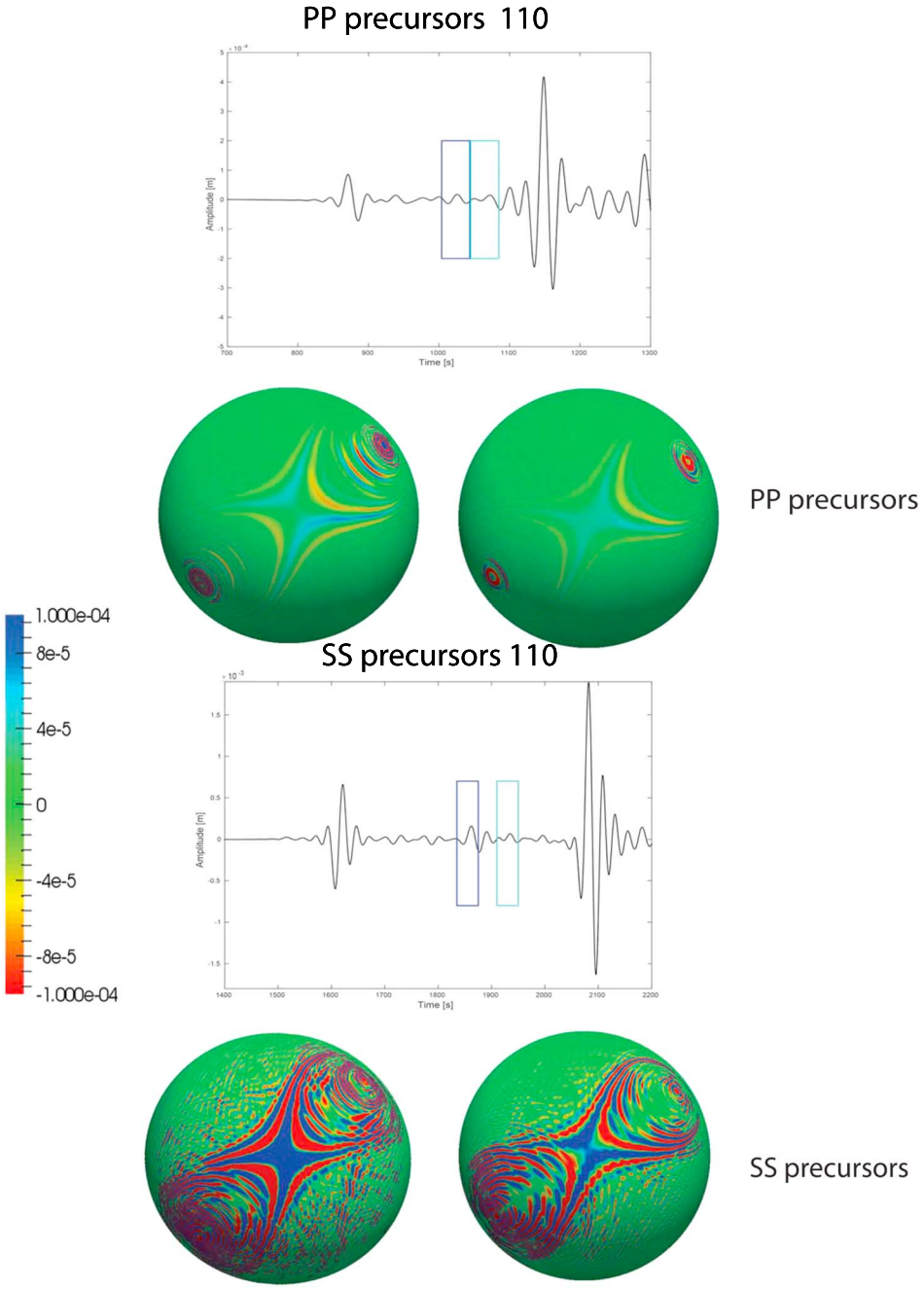

Figure 5. Record section of synthetic vertical components generated using PREM within the range 80–160° . The green and brown lines follow the ray theoretical arrivals of the *P670P* and *P400P* precursors, respectively, as calculated by TauP (Crotwell et al., 1999). The blue line represents the traveltime curve of the *P*, P_{diff} phases, and the purple line corresponds to the *PP* phase. No distinct, isolated arrivals of the *P400P* or *P670P* precursors are seen in any subrange.

such techniques may prove useful, they can only be applied to the limited regions with a dense station coverage.

Another important observation from the volumetric kernels is that the precursors are equally sensitive to both shear (V_{SV}) and compressional (V_P) mantle structure. A way to quantify the ratio between sensitivity to V_P over V_{SV} is to calculate the total energy of the kernel in the mantle. Doing that for seismograms at 90–150° distance, we observe that the ratio is about three. Given that current Earth models show that $\frac{dlnV_S}{dlnV_P} \sim 2$, we can conclude that the shear wave speed sensitivity of *PP* precursors is almost as important as the one for compressional wave speed (see details in the supporting information).

The strong sensitivity to both V_P and V_{SV} is due to the multiple conversions from *P* to *S* wave energy when the waves interact with internal discontinuities. Near source and receiver reflections are also major contributors to the sensitivity. Primary seismic phases, *PKP* and *P* or P_{diff}, complicate these kernels to a greater extent. Taking these observations into account, traveltime corrections become almost impossible, and interpretations in terms of boundary structure difficult. The joint sensitivity to upper-mantle discontinuities and structure can only be taken into account properly in a full waveform approach.

The low amplitude of the boundary sensitivity of the *PP* precursors is best seen by comparing them to the corresponding *SS* precursors. We plotted both sets of boundary kernels in Figure 4 on the same scale. The figure indicates that the sensitivity of *PP* precursor traveltimes is almost an order of magnitude lower than that of the *SS* precursors for the same source-receiver pair and the same source mechanism. Part of this could be due to the chosen source. The sensitivity kernels are cross-correlations of (adjoint) wavefields and (adjoint) strain deviators (Tromp et al., 2005). If the radiation pattern played a role, this would also affect the volumetric kernels, which it does not (compare Figure 2 with the corresponding figure in Koroni et al., 2017). Therefore, there are other effects, unrelated to the source and most likely due to wave interference, which reduce the *PP* precursor sensitivity kernels to the boundaries by about an order of magnitude.

The boundary kernels shown here and in the supporting information demonstrate that for some epicentral distances the sensitivity of the traveltime is zero at the ray theoretical reflection point. This is observed only for the *P670P* precursor in almost half the cases considered in our analysis. This finding is in agreement with the observation that the *P670P* precursor is frequently undetected in real data. To further investigate this, we calculated the reflection coefficients, as given in Aki and Richards (2002), of the *P400P* and *P670P* precursors, as well as those of *S400S* and *S670S* (see the supporting information). We find that the *P400P* and *P670P* reflection coefficients are of comparable value. Therefore, the poorer detectability of *P670P* compared to *P400P* cannot be attributed to the reflection coefficient but is related to wavefield effects. We further observe that the reflection coefficients of the *PP* precursors are typically twice as small as those of the *SS* precursors. The associated amplitude difference may explain a part of the difference in boundary sensitivity between the *PP* and *SS* precursors. However, it is likely that other wave phenomena contribute to the order of magnitude difference in boundary sensitivity between the *PP* and *SS* precursors.

Despite the narrow time windows around the predicted arrivals of *P400P* and *P670P* precursors, we see that wave interference dominates the sensitivity of their traveltimes. In fact, we see that the precursory phases are not easily observed and that they are almost always masked by other phases. This is independent of the chosen source time function and the frequency content.

To comprehensively address the dependence on the frequency of the data, we computed the sensitivity to compressional and shear wave speed for seismograms with different dominant frequencies. The general observation of significant wave interference and sensitivity to both compressional and shear wave speed does not change, as can be seen in the figures provided in the supporting information.

To check the effect of topography and of 3-D structure on the sensitivity kernels, we computed kernels for PREM with topography using the model of Meier et al. (2009) scaled by a factor of 2 and for S20RTS (Ritsema et al., 1999). The resulting kernels present very few differences and do not change any of our main conclusions (see the supporting information).

5. Conclusions

We presented an extensive analysis of finite frequency sensitivity of *PP* precursor traveltimes, which explains the diverging observations in the literature. The main conclusions of our sensitivity analysis of *PP* precursors traveltimes are as follows:

- There is considerable interference of various mantle and core phases within the *PP* precursor time windows.
- The precursor traveltimes are equally sensitive to compressional and shear wave speed structure.
- The strong wave interference is the likely reason that the precursors are barely sensitive to the boundary structure itself. In almost 50% of the cases examined, for a wide range of epicentral distances, the *P670P* traveltime sensitivity is close to zero at the location of the bounce point.

We therefore urge caution in interpreting topographic models based on the ray theoretical analysis of *PP* precursor traveltimes. We recommend to use *PP* precursor data only in the context of full waveform inversion.

Acknowledgments
The data used in this study are available via http://www.geo.uu.nl/~jeannot/My_web_pages/Downloads.html. The figures were created using ParaView (Ayachit, 2015) and ObsPy (Krischer et al., 2015). The research leading to these results has received funding from the European Research Council under the European Union's Seventh Framework Programme (FP/2007-2013)/ERC grant agreement 320639 (iGEO) and the European Union's Horizon 2020 Research and Innovation Programme (grant agreement 714069).

References

Aki, K., & Richards, P. G. (2002). *Quantitative seismology, theory and methods*. Sausalito, CA: University Science Books.
Ayachit, U. (2015). The ParaView guide: A parallel visualization application, Kitware.
Bina, C. R., & Helffrich, G. (1992). Calculation of elastic properties from thermodynamic equation of state principles. *Annual Review of Earth and Planetary Sciences*, *20*, 527–532.
Bolt, B. A. (1970). *PdP* and *PKiKP* waves and diffracted *PcP* waves. *Geophysical Journal of the Royal Astronomical Society*, *20*(4), 367–382. https://doi.org/10.1111/j.1365-246X.1970.tb06080.x
Chaljub, E., & Tarantola, A. (1997). Sensitivity of *SS* precursors to topography on the upper-mantle 660-km discontinuity. *Geophysical Research Letters*, *24*(21), 2613–2616.
Chambers, K., Deuss, A., & Woodhouse, J. H. (2005a). Reflectivity of the 410-km discontinuity from PP and SS precursors. *Journal of Geophysical Research*, *110*, B02301. https://doi.org/10.1029/2004JB003345
Chambers, K., Woodhouse, J. H., & Deuss, A. (2005b). Topography of the 410-km discontinuity from PP and SS precursors. *Earth and Planetary Science Letters*, *235*, 610–622.
Crotwell, H. P., Owens, T. J., & Ritsema, J. (1999). The TauP ToolKit: Flexible seismic travel-time and raypath utilities. *Seismological Research Letters*, *70*, 154–160.
Dahlen, F.-A., Hung, S.-H, & Nolet, G. (2000). Fréchet kernels for finite frequency traveltimes—I. theory. *Geophysical Journal International*, *141*, 157–174.
Davies, D., Kelly, E. J., & Filson, J. R. (1971). Vespa process for analysis of seismic signals. *Nature Physical Science*, *232*, 8–13.
Deuss, Arwen (2009). Global observations of mantle discontinuities using *SS* and *PP* precursors. *Survy Geophysics*, *30*, 301–326.
Deuss, A., Redfern, S. A. T., Chambers, K., & Woodhouse, J. H. (2006). The nature of the 660-kilometer discontinuity in Earth's mantle from global seismic observations of PP precursors. *Science*, *311*, 198–201.
Dziewoński, A. M., & Anderson, D. L. (1981). Preliminary reference Earth model. *Physics of the Earth and Planetary Interiors*, *25*, 297–356.
Estabrook, C. H., & Kind, R. (1996). The nature of the 660-kilometer upper-mantle seismic discontinuity from precursors to the *PP* phase. *Science*, *274*(5290), 1179–1182.
Flanagan, M., & Shearer, P. (1998). Global mapping of topography on transition zone velocity discontinuities by stacking *SS* precursors. *Journal of Geophysical Research*, *103*, 2673–2692.
Flanagan, M., & Shearer, P. (1999). A map of topography of 410-km discontinuity from *PP* precursors. *Geophysical Research Letters*, *26*(5), 549–552.
Helffrich, G. (1999). Thermal variations in the mantle inferred from 660 km discontinuity topography and tomographic wave speed variations. *Geophysical Journal International*, *151*(3), 935–943.
Helffrich, G., & Bina, C. R. (1994). Frequency dependence of the visibility and depths of mantle seismic discontinuities. *Geophysical Research Letters*, *21*(24), 2613–2616.
Husebye, E., & Madariaga, R. (1970). The origin of precursors to core waves. *Bulletin of the Seismological Society of America*, *60*(3), 939–952.
Jeanloz, R., & Thompson, A. B. (1983). Phase transitions and mantle discontinuities. *Reviews of Geophysics*, *1*(21), 51–74.
King, D. W., Haddon, R. A. W., & Husebye, E. S. (1975). Precursors to PP. *Physics of the Earth and Planetary Interiors*, *10*(2), 103–127.
Komatitsch, D. (2003). Advanced numerical modeling in geophysics (Modélisation numérique avancée pour la géophysique) (PhD thesis). (114 pp.). Pau, France. Habilitation Thesis (Habilitation à Diriger des Recherches, H.D.R.).
Komatitsch, D., & Tromp, J. (2002a). Spectral-element simulations of global seismic wave propagation—I. Validation. *Geophysical Journal International*, *149*(2), 390–412.
Komatitsch, D., & Tromp, J. (2002b). Spectral-element simulations of global seismic wave propagation—II. 3-D models, oceans, rotation, and self-gravitation. *Geophysical Journal International*, *150*(1), 303–318.
Koroni, M., Bozdağ, E., Paulssen, H., & Trampert, J. (2017). Sensitivity analysis of seismic waveforms to upper-mantle discontinuities using the adjoint method. *Geophysical Journal International*, *210*, 1965–1980.
Koroni, M., & Trampert, J. (2016). The effect of topography of upper mantle discontinuities on *SS* precursors. *Geophysical Journal International*, *204*, 667–681.
Krischer, L., Megies, T., Barsch, R., Beyreuther, M., Lecocq, T., Caudron, C., & Wassermann, J. (2015). ObsPy: A bridge for seismology into the scientific python ecosystem. *Computational Science & Discovery*, *8*, 014003.
Lessing, S., Thomas, C., Rost, S., Cobden, L., & Dobson, D. P (2014). Mantle transition zone structure beneath India and Western China from migration of *PP* and *SS* precursors. *Geophysical Journal International*, *197*, 396–413.
Lessing, S., Thomas, C., Saki, M., Schmerr, N., & Vanacore, E. (2015). On the difficulties of detecting PP precursors. *Geophysical Journal International*, *201*, 1666–1681.
Marquering, H., Nolet, G., & Dahlen, F. A. (1998). Three-dimensional waveform sensitivity kernels. *Geophysical Journal International*, *132*, 521–534.
Marquering, H., Nolet, G., & Dahlen, F. A. (1999). Three-dimensional sensitivity kernels for finite-frequency traveltimes: The banana-doughnut paradox. *Geophysical Journal International*, *137*, 805–815.
Meier, U., Trampert, J., & Curtis, A. (2009). Global variations of temperature and water content in the mantle transition zone from higher mode surface waves. *Earth and Planetary Science Letters*, *282*, 91–101.
Neele, F., & de Regt, H. (1999). Imaging upper-mantle discontinuity topography using underside-reflection data. *Geophysical Journal International*, *137*, 91–106.
Neele, F., de Regt, H., & VanDecar, J. (1997). Gross errors in upper-mantle discontinuity topography from underside reflection data. *Geophysical Journal International*, *129*, 194–204.
Neele, F., & Snieder, R. (1992). Topography of the 400 km discontinuity from observations of long-period P400P phases. *Geophysical Journal International*, *109*, 670–682.
Ritsema, J., Van Heijst, H. J., & Woodhouse, J. H. (1999). Complex shear velocity structure imaged beneath Africa and Iceland. *Science*, *286*, 1925–1928.

Rost, S., & Thomas, C. (2002). Array seismology: Methods and applications. *Reviews of Geophysics*, *40*(3), 1008. https://doi.org/10.1029/2000RG000100

Rost, S., & Thomas, C. (2009). Improving seismic resolution through array processing techniques. *Survey Geophysics*, *30*, 271–299.

Rost, S., & Weber, M. (2002). The upper mantle transition zone discontinuities in the Pacific as determined by short-period array data. *Earth and Planetary Science Letters*, *204*(3), 347–361.

Schimmel, M. (1997). Distinct body wave phenomena caused by mantle structure. UU Theses Archive, https://dspace.library.uu.nl/bitstream/1874/315006

Schmerr, N., & Thomas, C. (2011). Subducted lithosphere beneath the Kuriles from migration of PP precursors. *Earth and Planetary Science Letters*, *311*, 101–111.

Schneider, S., Thomas, C., Dokht, R. M. H., Gu, Y. J., & Chen, Y. (2018). Improvement of coda phase detectability and reconstruction of global seismic data using frequency-wavenumber methods. *Geophysical Journal International*, *212*(2), 1288–1301.

Shearer, P., & Flanagan, M. (1999). Seismic velocity and density jumps across the 410- and 660-kilometer discontinuities. *Science*, *285*, 1545–1548.

Talagrand, O., & Courtier, P. (1987). Variational assimilation of meteorological observations with the adjoint vorticity equation. I: Theory. *Quarterly Journal of the Royal Meteorological Society*, *113*, 1311–1328.

Tarantola, A. (1984). Inversion of seismic reflection data in the acoustic approximation. *Geophysics*, *49*, 1259–1266.

Tarantola, A. (1987). *Inverse problem theory: Methods for data fitting and modelparameter estimation*. Amsterdam, Netherlands: Elsevier Science Publishers.

Tarantola, A. (1988). Theoretical background for the inversion of seismic waveforms, including elasticity and attenuation. *Pure and Applied Geophysics*, *128*, 365–399.

Thomas, C., & Billen, M. I. (2009). Mantle transition zone structure along a profile in the SW Pacific: Thermal and compositional variations. *Geophysical Journal International*, *176*(1), 113–125.

Tromp, J., Tape, C., & Liu, Q. (2005). Seismic tomography, adjoint methods, time reversal and banana-doughnut kernels. *Geophysical Journal International*, *160*(1), 195–216.

Wajeman, N. (1988). Detection of underside P reflections at mantle discontinuities by stacking broadband data. *Journal of Geophysical Research*, *15*, 669–672.

Ward, S. N. (1978). Long-period reflected and converted upper-mantle phases. *Bulletin of the Seismological Society of America*, *68*(1), 133.

Wright, C. (1972). Array studies of seismic waves arriving between P and PP in the distance range 90° to 115°. *Bulletin of the Seismological Society of America*, *62*, 385–400.

Wright, C., & Muirhead, K. J. (1969). Longitudinal waves from the Novaya Zemlya nuclear explosion of October 27, 1966, recorded at the Warramunga seismic array. *Journal of Geophysical Research*, *74*(8), 2034–2048.